Colloids and Surfaces A: Physicochemical and Engineering Aspects 685 (2024) 133210

Contents lists available at ScienceDirect

Colloids and Surfaces A: Physicochemical and Engineering Aspects

journal homepage: www.elsevier.com/locate/colsurfa

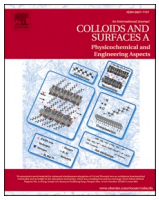

Phenazine-based conjugated microporous polymers: Influence of planarity and imine content on energy storage performance

Mohammed G. Kotp, Shiao-Wei Kuo, Ahmed F.M. EL-Mahdy *

Department of Materials and Optoelectronic Science, National Sun Yat-Sen University, Kaohsiung 80424, Taiwan

HIGHLIGHTS

- Innovative synthesis of redox-active CMPs based phenazine and various linkers.
- Thermal stability and improved surface areas in the designed CMPs.
- Planarity and imine content: influencers of supercapacitor performance.
- Incorporation of high planar and redox dynamic units modulate capacitance remarkably within our designed CMPs.
- Exceptional cycling stability of QP CMPs.

GRAPHICAL ABSTRACT

We report a rational design of conjugated microporous polymers (CMPs) based dynamic phenazine block which exhibit tunable capcitances with a comparable performance.

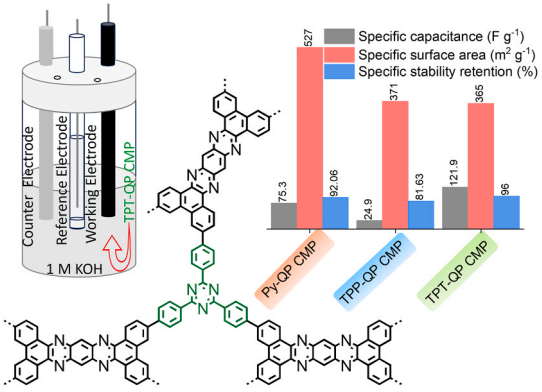

ARTICLE INFO

Keywords:
Conjugated microporous polymers
Phenazine
Pseudocapacitance
Electric double layer capacitance

ABSTRACT

Conjugated microporous polymers (CMPs) have been extensively employed across diverse applications. Nevertheless, there remains a necessity for more advancements in the fields of CMP-based supercapacitor electrodes. In this study, we present the synthesis of three redox-active phenazine based-CMPs through the coupling of redox-active 3,6,14,17-tetrabromodibenzo[*a*,*c*]dibenzo[5,6:7,8]quinoxalino[2,3-*i*]phenazine (QP-4Br) with various linkers of 1,3,6,8-tetrakis(4,4,5,5-tetramethyl-1,3,2-dioxaborolan-2-yl)pyrene (Py-4Bor), 2,4,6-tris(4-(4,4,5,5-tetramethyl-1,3,2-dioxaborolan-2-yl)phenyl)pyridine (TPP-3Bor), and 2,4,6-tris(4-(4,5-dimethyl-1,3,2-dioxaborolan-2-yl)phenyl)– 1,3,5-triazine (TPT-3Bor) those possess various degree of planarity and imine contents. Output CMPs display high thermal stability with char yields of up to 82.5% and improved surface areas of up to 527.22 m^2 g^{-1}. Interestingly, the ability to modulate the performance of energy storage and the mechanism of energy storage is influenced by the variability in the degree of planarity and imine contents of the linkers. The TPT-QP CMP has superior planarity and imine content, resulting in exceptional specific capacitance and energy density values of 121.9 F g^{-1} and 16.93 Wh Kg^{-1}, respectively. Further, it shows high specific capacitance

* Corresponding author.
E-mail address: ahmedelmahdy@mail.nsysu.edu.tw (A.F.M. EL-Mahdy).

https://doi.org/10.1016/j.colsurfa.2024.133210
Received 21 November 2023; Received in revised form 26 December 2023; Accepted 8 January 2024
Available online 11 January 2024

retention, recording 96% after 5000 cycles, and then their capacitances are comparable to other earlier reported porous materials. This research presents an effective approach for developing electrochemical redox CMPs to advance supercapacitor technology in the future.

1. Introduction

Nowadays, energy storage ability is the evaluation of economic progress considering the endeavor of states toward achieving sustainable development [1–3]. Consequently, countries motivate the research on these critical points, finding dynamic and economic solutions for energy storage and encouraging achieving a breakthrough in this field [4–7]. Supercapacitors are considered a significant technology for storing energy due to their acceptable power density, cyclability, reproducibility, and rapid charge/discharge (simple kinetics) [8,9]. These fruitful properties qualify supercapacitors as the main part of various sensitive instruments, for example, cameras, wind turbines, flywheels, electric cars, and braking systems [10–13]. Realistically, supercapacitors have a couple of techniques for storing charges; the first is faradic, which depends on redox reactions (pseudocapacitance) onto the electrode surface [14,15]. The other depends on electrochemical double-layer capacitance (EDLC), including ion adsorption/desorption within the charging/discharging processes occurring during the electrode/electrolyte interface, called the non-faradic technique [16,17]. Usually, pseudocapacitors display improved specific capacitance compared to EDLC systems [18–20]. Of note, three critical parameters can influence charge storage processes in supercapacitors: (I) charge separation from carbon electrode surface (activated carbon), (II) reaction onto the outer surface of electrode material, and (III) electrode/electrolyte interactions [21,22].

Therefore, supercapacitor features are greatly influenced by active electrode materials' composition and chemical properties [23–26]. Historically, pseudocapacitors incorporate transition metal oxides such as magnetite, while EDLC supercapacitor systems incorporate electrodes of carbon, graphene, or nanofibers [27–29]. Polymeric electrodes such as polyaniline, polypyrrole, polythiophene, and crosslinked polymers found an enormous interest in energy storage due to their significant redox properties, low energy consumption, and ecofriendly [30–35]. Polymeric materials-based Schiff-base reactions can incorporate redox-active units [36–39]. Schiff-base polymers have outstanding flexibility in terms of chemical properties since the wide diversity of dynamic monomers incorporated [40,41]. However, innovation and clear characterization of these families are still challenging. Consequently, innovating and constructing modulated porous matters that have high conductivity as well as pseudocapacitive properties are important to improve supercapacitance behaviors [42]. Sustainable development requires using sustainable and cost-effective materials; thus, organic polymeric materials obtain potential interest for supercapacitor fabrication.

Conjugated microporous polymers (CMPs) are considerable organic porous matters employed vastly for supercapacitors due to their porous farmwork and other inspiring features [43–50]. CMPs hold covalent bond structures, conjugated framework, improved surface area, tunable porosity, thermal stability, and easy functionalization [51,52]. Consequently, CMPs are utilized for numerous dynamic fields like that gas probes, photocatalysis, solar panels, gas adsorption, heterogeneous catalysis, and energy storage [45,53]. Their employment as supercapacitor electrodes still needs to be improved due to lower conductivity, hence lower specific capacitance [12,54–56]. Mixing CMPs with conducting moieties could improve the conductivity, but poor connection between these mixes can reduce their performance [57,58]. Notably, such inclusion of conductive additives is beneficial for enhancing conductivity, but these additives are non-redox-active which negatively impacts the volumetric energy density of the supercapacitor, which is deemed undesirable [54]. However, incorporating reactive monomers such as anthraquinone, aza aryls, ferrocene, porphyrin, or phenazines within CMP frameworks could be an alternative improvement way. This aims to enhance the conductivity of CMPs during their architectural construction. Briefly, through integrating these redox-active elements into the CMP frameworks, the overall conductivity of the polymers is expected to increase. This is crucial for the performance of supercapacitors, as higher conductivity facilitates the rapid movement of charge carriers, resulting in improved energy storage and release capabilities [59,60]. Although introducing these redox moieties incorporating CMPs is effective, modulation of their capacitance behavior is still challenging. Moreover, developing superior performance requires carefully selecting these redox active moieties to achieve improved conductivity and capacitance retentions.

Recently, phenazines have been stated as anthracene derivatives, which achieve superior electrochemical behavior close to quinone molecules [61,62]. This performance is revealed due to incorporating numerous redox active site-based structures of the phenazines similar to anthraquinones. Further, molecules-based phenazine predominantly reduces *via* couple-electron mechanism or proton coupling technique within electron transfer. Historically, the feature of the phenazine functional units could tune their redox activity [63]. For instance, Hollas et al. [64] declared that functionalizing phenazine with OH, sulfonate, or carboxylate groups could tune their redox performance. Wang et al. [65] stated that redox voltages of phenazine materials incorporated in redox flow battery could be tuned *via* functionalization by OH and amino units; moreover, considering the position of OH groups can also affect the performance. Therefore, in the light of sustainable development, incorporating phenazine into CMPs can tune their performance in energy storage.

In this study, we emphasize the design of three CMPs based on the coupling of redox-active 3,6,14,17-tetrabromodibenzo[*a*,*c*]dibenzo[5,6:7,8]quinoxalino[2,3-*i*]phenazine (QP-4Br) with 1,3,6,8-tetrakis(4,4,5,5-tetramethyl-1,3,2-dioxaborolan-2-yl)pyrene (Py-4Bor), 2,4,6-tris(4-(4,4,5,5-tetramethyl-1,3,2-dioxaborolan-2-yl)phenyl)pyridine (TPP-3Bor), and 2,4,6-tris(4-(4,5-dimethyl-1,3,2-dioxaborolan-2-yl)phenyl)− 1,3,5-triazine (TPT-3Bor) and then deriving Py-QP, TPP-QP, and TPT-QP CMPs respectively *via* classical Suzuki coupling protocol (Scheme 1). Notably, Triazine rings are generally planar structures and Triphenyl triazine (TPT), with its three phenyl groups attached to the triazine core, maintains a high degree of planarity. Therefore, such presence of three phenyl rings reinforces planarity, as the conjugation across the entire structure helps maintain a flat geometry [66]. On the other hand, Pyridine is a six-membered aromatic ring with a nitrogen atom, triphenyl pyridine, with three phenyl groups attached to the pyridine ring, may exhibit a degree of planarity, but the presence of three phenyl groups can influence the planarity of triphenyl pyridine. The steric effects of these groups may introduce some deviations from perfect planarity as we early reported et al. [46]. On the other scale, Pyrene is a polycyclic aromatic hydrocarbon with four fused benzene rings, while the individual rings are planar, the fusion of these rings introduces some distortion, but pyrene is relatively planar compared to more complex structures, and its planarity can be influenced by substituents and the surrounding environment [46,67]. Therefore, these boronic molecules vary in their imine content and planarity. Our set of QP CMPs displays improved thermal stabilities recording higher char yields of 82.5%, modulated pores and improved surface areas up to 527.22 m^2 g^{-1}, as well as smooth topologies. We emphasized the dynamic power of their imine inclusions, building unit planarity onto their physicochemical features, and suitability as supercapacitor electrodes. Thus, we employed these QP CMPs as supercapacitor electrodes. Studies

of electrochemical charge/discharge reveal that the specific energy storage onto the QP CMPs follows the faradic model at different rates; thus, the faradic mechanism depends mostly on the imine contents of this electrode nature. Moreover, highly planar units derived improved specific capacitances. Furthermore, galvanostatic charge/discharge models reveal that the maximum specific capacitance of TPT-QP CMP reached up to 121.9 F g^{-1}, exceeding the capacitance of the early reported porous matters used as supercapacitor electrodes. We discussed the mechanism of the faradic redox reaction of the TPT-QP CMP overcharging and discharging process.

2. Experimental

2.1. Materials

Initial chemicals and solvents conducted for experiments without further purification. Indeed, we used an array of analytical grade substances in our research. For example, Combi-Blocks (San Diego, USA) provided the bis(pinacolato)diboron (98%), [1,1′-bis(diphenylphosphino)ferrocene]dichloropalladium(II) (dppf, 95%), potassium hydroxide grains, and potassium acetate (98%). Acros Organics (Geel, Belgium) supplied tetrakis (triphenylphosphine)palladium (99%) and potassium carbonate (K_2CO_3, 99%). J. T. Baker (Radnor, USA) supplied dioxane (anhydrous, 99.8%) and dimethylformamide (DMF, anhydrous, 99.8%). The entire set of experiments relied on DI water.

2.2. Characterizations

Numerous instruments were employed to elucidate the building monomers, CMPs, and electrochemical properties. Detailed information, including their models, is provided in the supporting information file.

2.3. Design of Monomers

To accomplish the design of Py-QP, TPP-QP, and TPT-QP CMPs, we synthesized numerous subunits including QP-4Br, Py-4Br, Py-4Bor, TPP-3Br, TPP-3Bor, TPT-3Br, and TPT-3Bor as reported earlier and then briefed in Schemes S1-4, also providing various check scans of FTIR, ^{1}H NMR, and ^{13}C NMR profiles (Figs S1-10).

2.4. Design of Py-QP CMP

Py-4Bor (0.24 mmol, 150 mg), QP-4Br (0.21 mmol, 170 mg), Pd$(PPh_3)_4$ (0.03, 40 mg), and K_2CO_3 (2.1 mmol, 294 mg) were mixed in Schlenk flask and then degassed for 15 min. After that, solvents of DMF (10 mL) and deionized water (1.25 mL) were charged to the reaction flask followed by three thaw turns, and then the tube was magnetically stirred for 72 h at 130 °C Scheme S5. Afterwards, the powder had been centrifuged and rinsed *via* hexane, methanol, acetone, and THF *via* the Soxhlet technique. Finally, the solid powder was dried overnight at 80 °C. FTIR (powder); 3056, 1641, 1591, and 1510 cm^{-1} (Fig. S2).

2.5. Design of TPP-QP CMP

In a Schlenk tube, the TPP-Bor (200 mg), Pd$(PPh_3)_4$ (50 mg), as well as QP-4Br (174.7 mg). Then, we charged the K_2CO_3 (303 mg, 30.0 mmol) into the reaction, degassed for 15 min as well. The cosolvent of DMF/water (10, 1.25 mL) was added to the reaction. These reaction

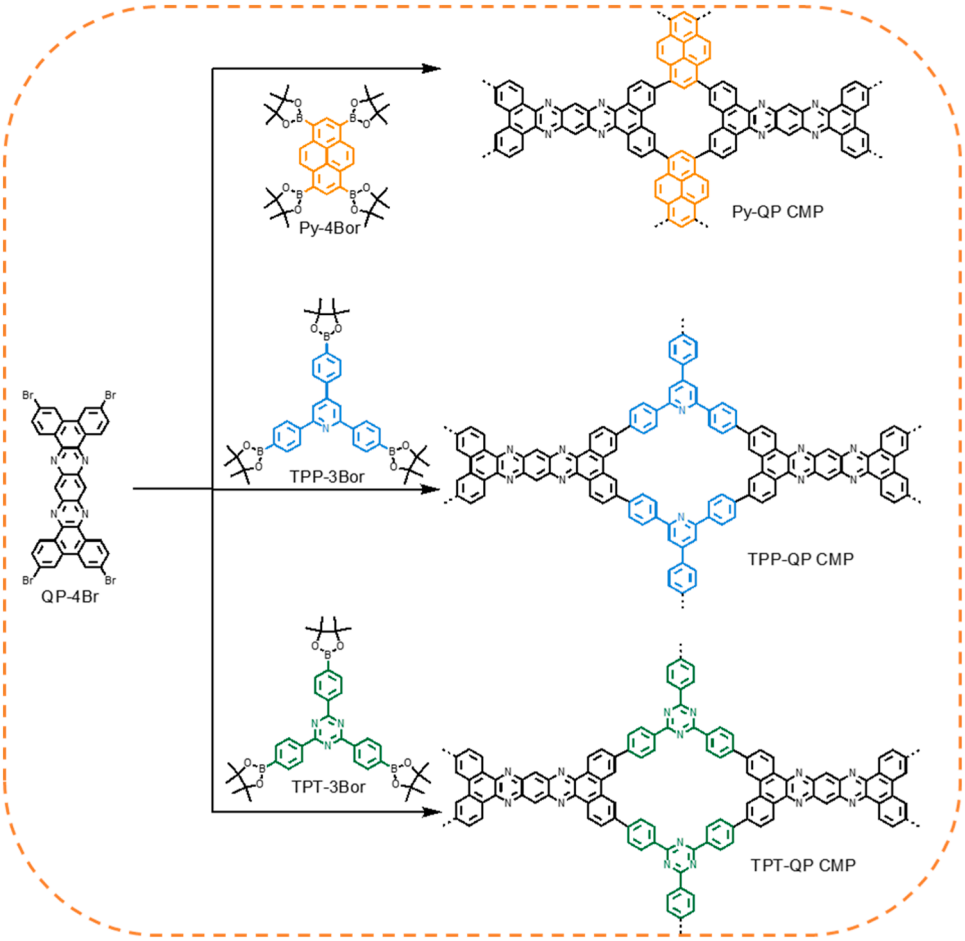

Scheme 1. Synthesis scheme of Py-QP, TPP-QP, and TPT-QP CMPs using Suzuki protocol catalyzed by Pd$(PPh_3)_4$ and solved into DMF/H_2O at 130 °C for three days.

ingredients were exposed to triple thaw turns then boiled for three days under N_2 pressure at 130 °C and gentle stirring Scheme S6. The brown powder was separated, rinsed for many turns *via* water, then deeply rinsed using the Soxhlet system *via* hexane, and MeOH, and then dried at 80 °C overnight. FTIR (powder): 1730, 1632 cm^{-1} (Fig. S3).

2.6. Design of TPT-QP CMP

In the Schlenk flask, QP-4Br (0.18 mmol, 150 mg), TPT-3Bor (0.2 mmol, 173 mg), $Pd(PPh_3)_4$ (0.04 mmol, 50 mg) and K_2CO_3 (1.8 mmol, 260 mg) were intermixed then degassed for 15 min. After that, the cosolvent of DMF/water (10, 1.25 mL) was charged to the reaction flask; then, three thaw cycles were performed for the reaction. The tube was left for three days at 130 °C under magnetic stirring Scheme S7. Afterward, the powder was filtered out and rinsed using the Soxhlet technique using methanol, hexane, acetone, and THF, then dried. FTIR (powder): 3001, 1632, 1600 and 1512 cm^{-1} (Fig. S4).

3. Results and discussion

3.1. Molecular Characterizations of CMPs

The textural properties and stabilities of CMP materials play pivotal roles in determining their suitability for various applications. These properties, including surface area, pore size distribution, and thermal stability, profoundly influence the materials' performance in areas such as gas storage, catalysis, and energy storage devices. The high surface areas of CMPs, often achieved through meticulous design and synthesis, contribute to enhanced adsorption capacities and catalytic activities. Furthermore, the control of pore size distribution is crucial for accommodating specific molecules or ions, imparting selectivity in separation or catalytic processes. Thermal stability is a key consideration for applications involving elevated temperatures, ensuring the structural integrity of CMPs over extended operational periods. Consequently, a comprehensive understanding and optimization of the textural properties and stabilities of CMP materials are essential for advancing their effectiveness in diverse applications within the realm of materials science [68]. Our triple CMPs frameworks of phenazine nominates Py-QP, TPP-QP, and TPT-QP CMPs were designed in a tolerable yield *via* classical coupling protocol of Suzuki [69] employing the dynamic linker of QP-4Br with three boronic esters of Py-4Bor, TPP-3Bor, and TPT-3Bor (Schemes S1-4) respectively solvated in a mixture of DMF, and aqua as well as catalyzed *via* palladium(0) at 130 °C. The resulting QP-CMPs exhibit low solubility in ordinary solvents such as ethanol, acetone, propanol, DMF, and THF, confirming their strong crosslinking. The molecular formulation of those designed QP-CMPs was demonstrated *via* infrared (FTIR), solid state ^{13}C NMR (SS NMR) scans as well. The FTIR spectrums of Py-QP, TPP-QP, in addition to TPT-QP CMPs features an entirely vanishing of characteristic absorption bands at 823 cm^{-1} emerging out C-Br groups based QP-4Br beside demise of absorption bands of B-O at 1373, 1399, and 1341 cm^{-1} for Py-4Bor, TPP-3Bor, and TPT-3Bor respectively (Figs. S2–4), implying the intercoupling of these constructing subunits. Demonstrated signals, however, at 1641, 1614, and 1632 cm^{-1}, for C═N units based phenazine units, and at 1591, 1542, and 1591 cm^{-1} due to the aryl alkene groups based Py-QP, TPP-QP, TPT-QP CMPs, respectively [44,45]. The SS NMR profiles of those as-designed Py-QP, TPP-QP, in addition to TPT-QP CMPs exhibit trait bands between 142 to 118 ppm, implying the aryl carbon nuclei of C═C and C═N [44,70].

Further, we conducted XPS measurements to emphasize the relative chemical formulation on CMP surfaces and the electronic valances of their carbons, nitrogens, and oxygens. Notably, nitrogenic sites based CMPs are able to generate molecular defects within those carbonous edges, consequently they can perform physical reactions with oxygen, forming oxygen-incorporating units subsequent to air exposure. The X-ray photoelectron spectroscopy (XPS) survey exhibits several oxygen dynamic groups seen from C-O connections in the C 1 s scan. The High-resolution sweeps of C 1 s, N 1 s, and O 1 s of those Py-QP, TPP-QP, and TPT-QP CMPs were investigated. Firstly, C1s spectrums of Py-QP, TPP-QP, as well as TPT-QP CMPs are disentangled into quadruple signals. The fitting outcomes of the C1s scan based Py-QP, TPP-QP, and TPT-QP CMP structures reveal the existence of certain carbon forms, including sp^2 carbon (C═C, 283.7 eV), sp^2 carbon interconnected nitrogen (C═N, 285.1 eV), carbons linked alcoholic oxygens (C-OH, 286.2 eV), as well as keto groups (C═O) (287.3 eV). The N1s spectra of the Py-QP CMP exhibits a unique featured peak at 400.8 eV, characteristic of pyridinic nitrogen of the phenazine ring. Otherwise, N1s scan of the TPP-QP and TPT-QP CMPs are deconvoluted into triple peaks, including hexagonal pyridinic-N atoms from pyridine and triazine rings respectively (397.9 eV), sp^2-nitrogens linked carbon atoms of hexagonal ring (400.7 eV) and N_2 (403.8 eV). Notably, the pyridinic-N has a quantitative presence within TPT-QP CMP. Furthermore, Py-QP, TPP-QP, and TPT-QP CMPs frameworks exhibit four types of oxygen within their surfaces at 532.5, 533.9, and 537.8 eV assignable to C═O/C-O-H/C-O-C groups, watrous oxygens, oxidized species at surface incorporating Na KLL, respectively [44,45].

The porosity of those designed Py-QP, TPP-QP, and TPT-QP CMPs were investigated at 77 K *via* the N_2 adsorption desorption isotherms. The obtained isotherms of Py-QP, TPP-QP, as well as TPT-QP CMPs represent a sharp ascent at reduced pressures, elucidating their microporosity features. The dynamic BET surface areas (S_{BET}) for Py-QP, TPP-QP, and TPT-QP CMPs are 527.2, 371, and 365.6 $m^2\ g^{-1,}$ respectively. The improved surface area of the Py-QP CMP over TPP-QP and TPT-QP CMPs reveals higher π-π stacking of Py-based CMPs than TPP and TPT ones [71]. Notably, the adsorbed N_2 amount increases gradually at a high P/P_0 close to 0.45, on the other hand, hysteresis loops persist to low pressures, implying the integration of model I and IV features thus together revealing the microporous and mesoporous feature. CMPs' pore sizes classifications were analyzed *via* nonlocal density functional theory (NLDFT) which exhibit those Py-QP CMP, TPP-QP CMP, as well as TPT-QP CMP include various pores sizes of 0.66, and 1.69, 1.13, and 1.84, and 0.63, 1.54 and 1.66 nm respectively. Notably, sharp desorption stages at P/P_o imply the cavitation of N_2, confirming these mesoporous obtain the geometry of an ink bottle. Moreover, mesoporous dimensions of Py-QP, TPP-QP, and TPT-QP CMPs are 3.22, 4.87, as well as 3.22 nm, respectively resulting because of elastic distortions of their porous frameworks or severe expanding into nitrogenic sites as reported before for various porous frameworks holding irregular mesopores. The total pore volumes (V_{total}) of Py-QP, TPP-QP, and TPT-QP CMPs are respectively 0.369, 0.5124, and 0.33 $cm^3\ g^{-1}$ (Table S1). Inspired these improved surface areas as well microporous features, these QP frameworks are considered a novel class of porous polymeric families as electrodes for energy storage. Their microporous kernel is presumably accessible to electrolyte molecules [44,45].

CMPs show high thermal stabilities; thus, thermal gravimetric analysis (TGA) was performed for our Py-QP, TPP-QP, and TPT-QP CMPs under a nitrogenic environment to clarify this important point. The decomposition temperature (T_d) of Py-QP, TPP-QP, as well as TPT-QP CMPs frameworks are 615, 625, and 591 °C, attaining 82.5%, 81.5%, and 76.5% respectively Table S1 [44,45]. This reinforced stabilities of Py-QP CMP exceeding TPP-QP and TPT-QP CMPs are conceivably due to the significant degree of fusion of pyrene subunits based the Py-QP framework, that improved π-π stacking among their zones. At all, high thermal stabilities of QP confirm their higher degree condensations [44, 45,72]. The morphologies of Py-QP, TPP-QP, as well as TPT-QP CMPs were studied *via* scanning electrons microscope (SEM), transmission electrons microscope (TEM) as well. According to observations as shown in Fig. 1a-c, the SEM visualizations attribute these Py-QP, TPP-QP, and TPT-QP CMPs frameworks hold some agglomerations. These agglomerated particles of Py-QP, TPP-QP, as well as TPT-QP CMPs are discernible using TEM visualizations (Fig. 1d-f).

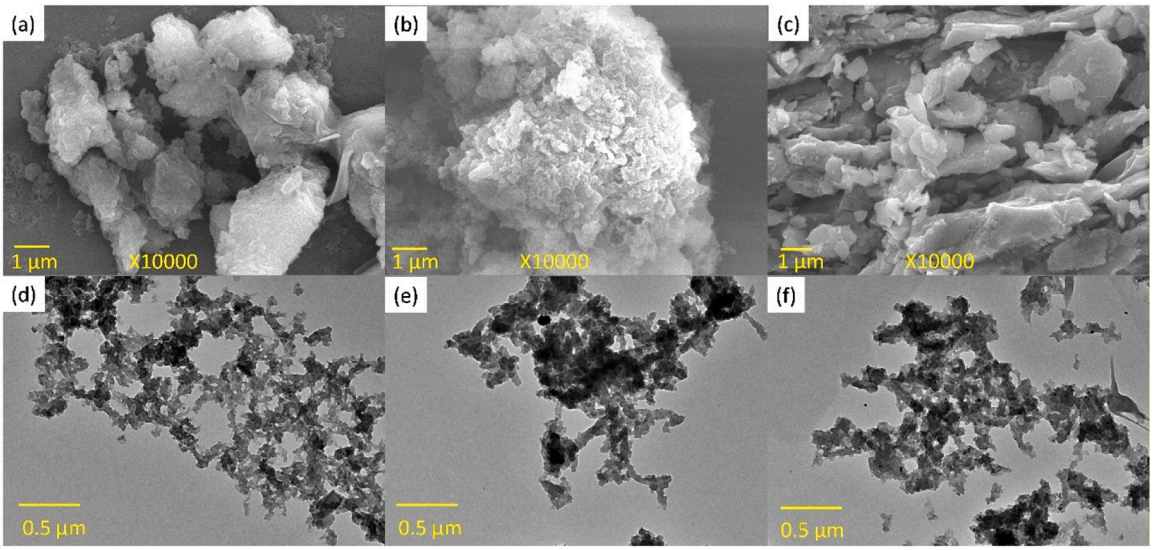

Fig. 1. FE-SEM (a-c), and TEM images (d-f) of Py-QP, TPP-QP, and TPT-QP CMPs respectively.

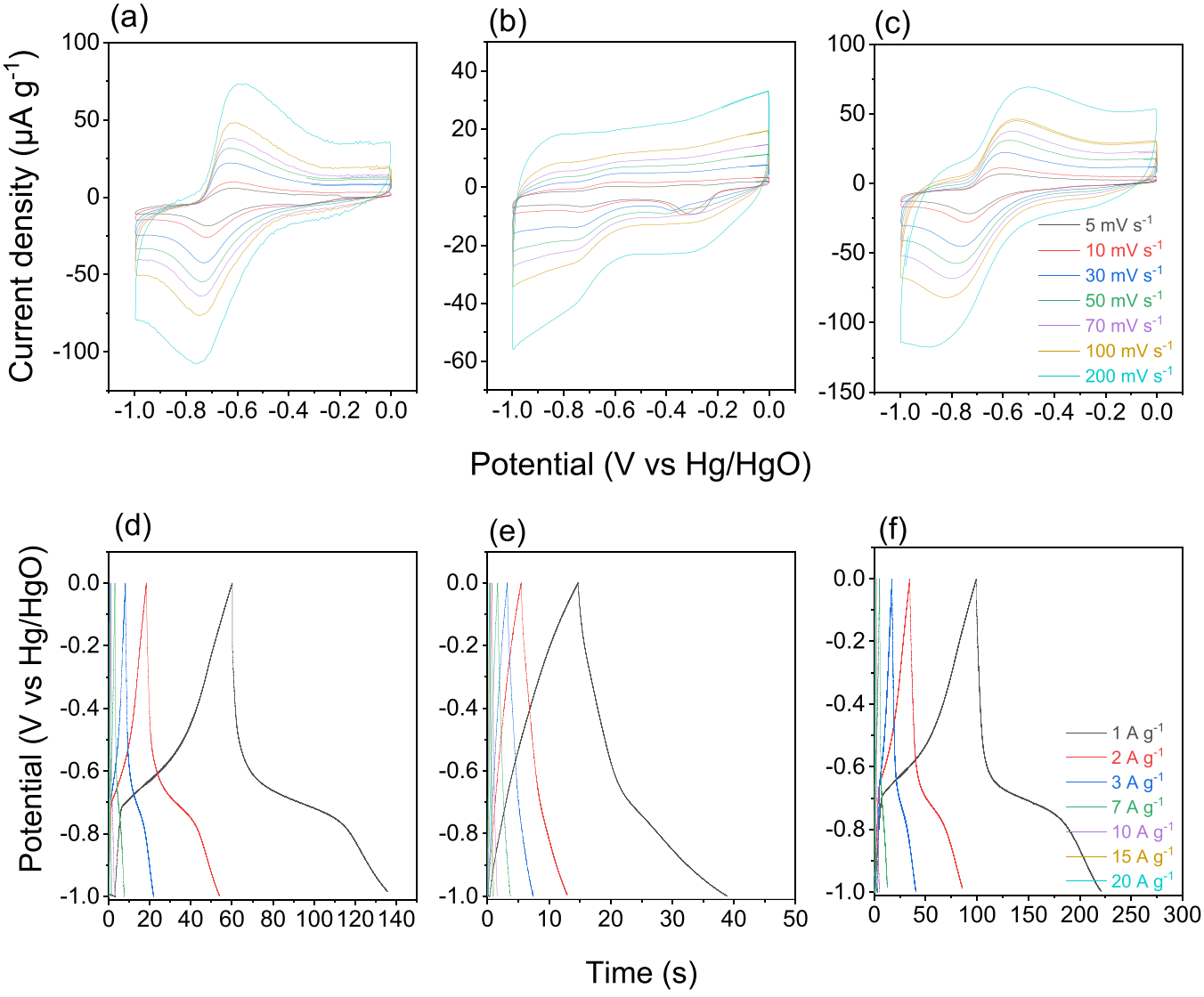

Fig. 2. Cyclic voltammetry curves of the (a) Py-QP, TPP-QP (b) and (b) TPT-QP CMPs at various sweep rates (mV s^{-1}). Galvanostatic charge-discharge curves (GCD) of the (d) Py-QP, (e) TPP-QP and (f) TPT-QP CMPs at different current densities (A g^{-1}).

3.2. Electrochemical Features

The electrochemical performance of Py-QP, TPP-QP, and TPT-QP CMPs was evaluated *via* cyclic voltammetry (CV) and GCD conductions in 1 M of aqueous electrolyte of KOH. Fig. 2a-c exhibit the corresponding CV plateaus of Py-QP, TPP-QP, and TPT-QP CMPs, respectively, which were conducted at different scan rates between 5 and 200 mV s^{-1} at voltage windows of 0 to − 1 V (V *vs.* Hg/HgO). These CV scans of Py-QP, TPP-QP, and TPT-QP CMPs exhibited rectangle plateaus, implying that capacitive performance is presumably due to the EDLC. Further, as observed in Fig. 2a and Fig. 2c, the Py-QP and TPT-QP CMPs provided relatively higher current densities than TPP-QP CMP, indicating their improved electrochemical performance. Furthermore, Py-QP and TPT-QP CMPs provided observable redox peaks within their CV scans than TPP-QP CMP, which presumably occur due to the incorporation of electron-rich aryl rings or nitrogenic units such as pyrazine. Moreover, fused polymeric moieties, including high conjugation such as py, derive high charge mobility and electron donating features, improving the capacitance performance. Therefore, we can reveal these improved current densities of Py-QP and TPT-QP CMPs over TPP-QP CMP due to the high planarity of the Py-QP CMP and high percentage of imine units based TPT-QP CMP [73,74]. Otherwise, pyridine has a lower planarity degree; hence, TPP-QP CMP thus shows lower current density. Moreover, higher scan rates derive higher current densities; however, CV plateaus still imply simple kinetics in addition to improved rate ability. Notably, a little shifting of oxidation and reduction peaks based on Py-QP and TPT-QP CMPs to positive and negative scales implies their input impedances (Fig. 2a, c). We scanned their validities toward galvanostatic charge-discharge for deep insight into electrochemical-specific capacitances of QP CMPs. Fig. 2d-f exhibits the GCD scans of Py-QP, TPP-QP, and TPT-QP CMPs swept at numerous densities of current ranging between 1 to 20 A g^{-1}. The GCD plateaus based Py-QP and TPT-QP have triangular forms with severe bending, confirming their pseudocapacitance and EDLC features. Otherwise, the GCD curve of TPP-QP CMP has a triangular shape with a little bend, confirming its higher effect due to EDLC. This behavior confirms the CV scan results, which are attributed to the high planarity of Py and redox phenazine units based on Py-QP CMP. Moreover, numerous redox sites of TPT-QP CMP located at triazine and phenazine blocks derived a high possibility of pseudocapacitance [75].

As detectable, the discharging periods of TPT-QP CMP are longer than those of Py-QP CMP and TPP-QP CMP (Fig. 2d-f), revealing the highest capacitance of the former. Therefore, we applied eqn. S1 to estimate specific capacitance based on these GCD scans (Fig. 3a). The dynamic capacitance of the TPT-QP CMP (121.9 F g^{-1}) which is superior to that of Py-QP framework (75.3 F g^{-1}), and TPP-QP CMP (24.9 F g^{-1}) when the current density is 1 A g^{-1}. Furthermore, Ragone plots (Fig. 3b) suggested that Py-QP, TPP-QP, and TPT-QP CMPs-based electrodes have superior energy densities up to 10.46, 3.45, and 16.93 Wh $Kg^{-1,}$ respectively. The little bit facilitated capacitance of TPT-QP CMP relative to those of Py-QP CMP or TPP-QP CMP is probably due to TPT blocks which offer higher imine percentages and extend π-electron conjugation, hence enhancing the electric conductivity of the derived TPT-QP CMP. Moreover, such a combination between a couple of redox building blocks as QP and TPT offers a higher degree of pseudocapacitance, where the redox process of QP and TPT entailed electrons reduction into anions of QP^{4-} and TPT^{2-} respectively Fig. 4a, b. Although the TPT-QP CMP has the lowest surface area, its specific capacitance is predominantly controlled *via* the faradic mechanism. Fig. 4c emphasizes that the QP and TPT could be reduced during discharge processes, while oxidations of QP^{4-} and TPT^{2-} anions occurred within the charging processes. The proposed mechanism of TPT-QP CMP matched well with the reported findings [76,77]. As reported in our earlier study, the Py-QP CMP shows slightly higher capacitance due to its planarity with the fused aryl structures as well as the prolonged π-conjugation [73]. Consequently, the dynamic charge-transfer ability-based pyrene subunit is taken advantage of a crucial component in the progression of charge-transfer based applications, especially electronic devices. The lower planarity of the TPP unit hinders the electron transport and limits the redox within TPP-QP CMP to some extent, thus displaying a little capacitance of 24.9 F g^{-1}.

Electrochemical impedance spectroscopies (EIS) conductions were carried out for deep insight into ions mobilities in addition to interior resistances corresponding to Py-QP, TPP-QP, and TPT-QP CMPs (Fig. 4d). Under low frequencies, EIS scans display vertical form confirming rapid charge transfer, and TPT-QP CMP exhibits the lowest ions diffusion resistances. As detected, intersections of semicircles at x-axis could be emphasized considering those equivalent series resistances (ESR), which consequently explains the interface resistance in between dynamic electrochemical moiety with the current collector and then the internal impedances of electrode and electrolyte. Py-QP and TPT-QP CMPs represent improved performances than TPP-QP CMP, whereas the formers have lower ESRs and are much closer to the Z'' axis. These detections elucidate the improved interactions at electrode-electrolyte

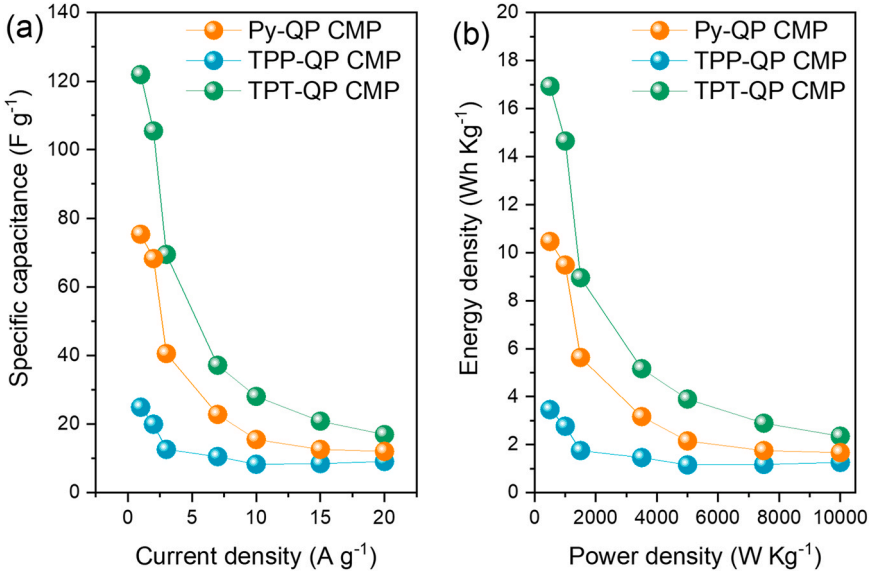

Fig. 3. Specific capacitances (a) and power densities (b) of the Py-QP, TPP-QP, and TPT-QP CMPs electrodes at different current densities (A g^{-1}).

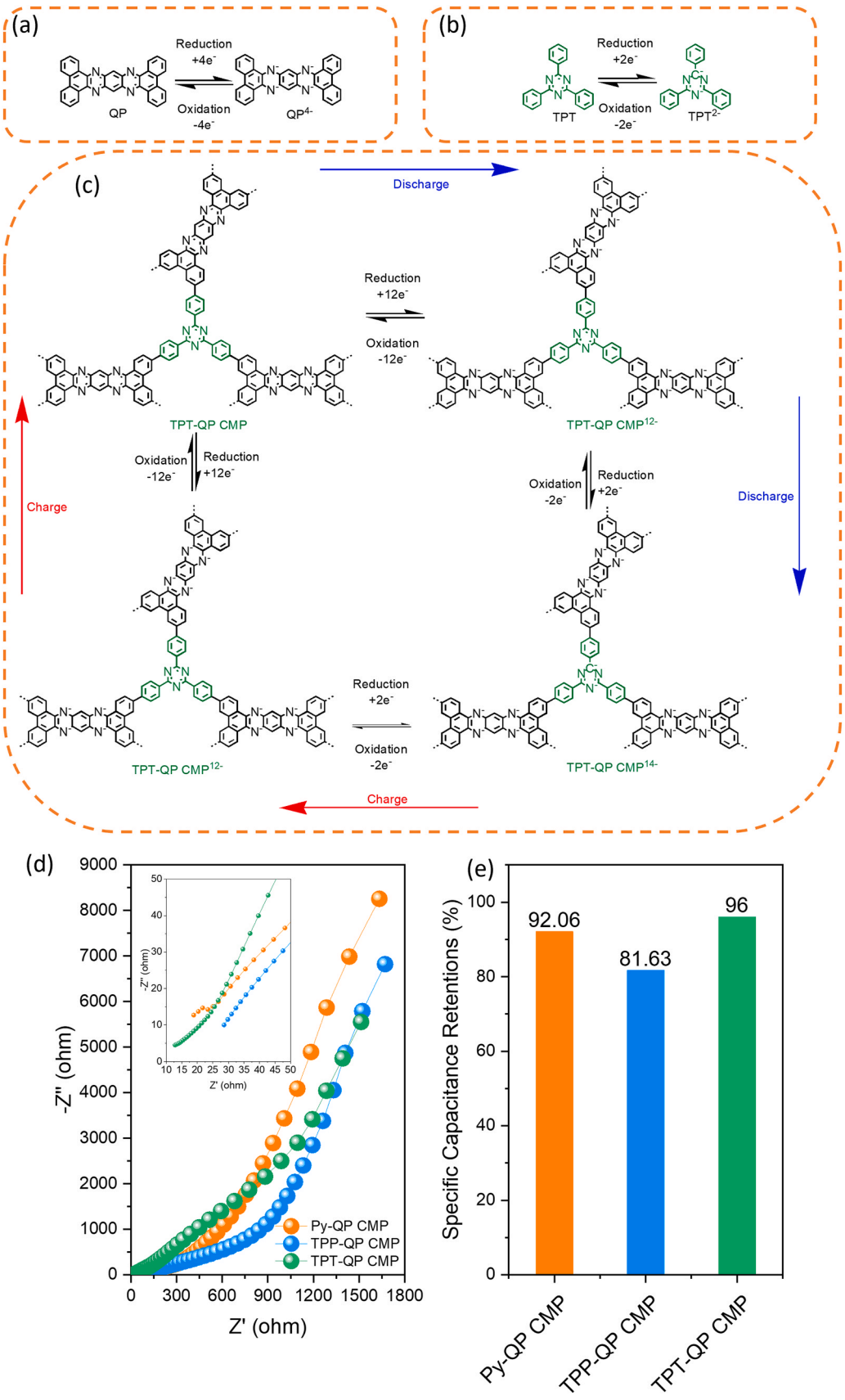

Fig. 4. Proposed redox processes of (a) QP, (b) TPT, and (c) TPT-QP CMP, Nyquist scans of the Py-QP, TPP-QP, and TPT-QP CMPs (d). Stability retentions of Py-QP, TPP-QP, and TPT-QP CMPs for 5000 cycles detected at current density of 10 A g^{-1} (e).

interfaces, hence rapid charge diffusions and higher conductivities of Py-QP and TPT-QP CMPs. Notably, high surface areas of QP CMPs offer higher interaction sites between electrode-electrolyte materials. Notably, nitrogenic and oxygen sites based CMPs improve their wettability degree and electrochemical performance. EIS scans reveal the initial resistance (cumulative impedances) of Py-QP, TPP-QP, and TPT-QP CMPs to be 18.84, 28.57, and 12.85 ohms, respectively. The lower impedance of TPT-QP CMP confirms its improved electrical conductivity, rendering it a potentially useful supercapacitor electrode. Also, various building blocks based on QP CMPs grant us tunable features. Hence, they could tune the electrical properties of polymeric supercapacitors.

Notably, The Py-QP, TPP-QP, and TPT-QP CMPs display highly comparable capacitance values than other reported porous materials such as BC-BF-CMP (260 F g^{-1} at 0.5 A g^{-1}) [13], BC-Py-CMP (211 F g^{-1} at 0.5 A g^{-1}) [13], TPA-Bz CMP (55.1 F g^{-1} at 1 A g^{-1}) [12], TPA-Py CMP (78 F g^{-1} at 1 A g^{-1}) [12], PTPA-25 (335 F g^{-1} at 0.5 A g^{-1}) [78], TPA–COF–1 (51.3 F g^{-1} at 0.2 A g^{-1}) [79], TPT–COF–4 (2.4 F g^{-1} at 0.2 A g^{-1}) [79], TPT–COF–6 (0.24 F g^{-1} at 0.2 A g^{-1}) [79], N-CMP (71 F g^{-1} at 1 A g^{-1}) [80], and CoPc-CMP (13.7 F g^{-1} at 1 A g^{-1}) [81], and other more porous materials as summarized in Table S2. Importantly, cycling over 5000 GCD scans at 10 A g^{-1} was conducted to detect the capacitance retention of QP CMPs (Fig. 4e). The Py-QP, TPP-QP, and TPT-QP CMPs represent excellent cycling stability with 92.06%, 81.63%, and 96% retention, respectively.

4. Conclusion

In summary, the redox-active phenazine unit was employed as a core unit with three monomers possessing various degrees of planarity and imine units toward designing three CMPs nominated Py-QP, TPP-QP, and TPT-QP CMPs. These QP-CMPs showed high thermal stabilities and improved surface areas. We discovered that Py-QP and TPT-QP CMPs with high planar Py and TPT units have better specific capacitance than TPP-QP CMPs with less planar TPP units, owing to facilitating rapid charge mobility between CMP layers. These Py-QP and TPT-QP CMPs improved the faradic process due to the redox active phenazine moiety plus their planar structures. On the other hand, the TPT-QP CMP with the highest imine content showed the highest specific capacitance due to the heteroatom effect, which improved the wettability and charge mobility. The resulting TPT-QP CMP displayed a high specific capacitance of up to 121.9 F $g^{-1,}$ exceeding the previously reported porous materials. The study offers a novel strategy for tuning phenazine-incorporated supercapacitor electrodes' capacitance and storage technique. Moreover, we provided a molecular engineering vision for CMP design toward dynamic supercapacitor electrodes with further possible modifications targeting higher efficiencies.

CRediT authorship contribution statement

Kuo Shiao-Wei: Validation, Resources, Investigation, Conceptualization. **Kotp Mohammed G.:** Writing – original draft, Software, Methodology, Formal analysis, Conceptualization. **EL-Mahdy Ahmed F. M.:** Writing – review & editing, Writing – original draft, Software, Project administration, Funding acquisition, Formal analysis, Data curation.

Declaration of Competing Interest

The authors declare that they have no known competing financial interests or personal relationships that could have appeared to influence the work reported in this paper.

Data Availability

Data will be made available on request.

Acknowledgements

This study was supported financially by the Ministry of Science and Technology, Taiwan, under contracts NSTC 112-2221-E-110-005-MY3, 111-2221-E-110-003, and 112-2218-E-110-007.

Appendix A. Supporting information

Supplementary data associated with this article can be found in the online version at doi:10.1016/j.colsurfa.2024.133210.

References

[1] M. Hannan, A.Q. Al-Shetwi, R. Begum, P.J. Ker, S. Rahman, M. Mansor, M. Mia, K. Muttaqi, Z. Dong, Impact assessment of battery energy storage systems towards achieving sustainable development goals, J. Energy Storage 42 (2021) 103040.
[2] U. Nzotcha, J. Kenfack, M.B. Manjia, Integrated multi-criteria decision making methodology for pumped hydro-energy storage plant site selection from a sustainable development perspective with an application, Renew. Sustain. Energy Rev. 112 (2019) 930–947.
[3] S.K. Pathak, V. Tyagi, K. Chopra, Kalidasan B, A. Pandey, V. Goel, A. Saxena, Z. Ma, Energy, exergy, economic and environmental analyses of solar air heating systems with and without thermal energy storage for sustainable development: A systematic review, J. Energy Storage 59 (2023) 106521.
[4] X. Chen, M. Zhang, S. Jiang, H. Gou, P. Zhou, R. Yang, B. Shen, Energy reliability enhancement of a data center/wind hybrid DC network using superconducting magnetic energy storage, Energy 263 (2023) 125622.
[5] R. Fallahifar, M. Kalantar, Optimal planning of lithium ion battery energy storage for microgrid applications: considering capacity degradation, J. Energy Storage 57 (2023) 106103.
[6] H. Liu, J. Jiang, Flywheel energy storage—an upswing technology for energy sustainability, Energy Build. 39 (2007) 599–604.
[7] H. Zhang, S. Gao, P. Zhou, Role of digitalization in energy storage technological innovation: evidence from China, Renew. Sustain. Energy Rev. 171 (2023) 113014.
[8] S. Nayak, A. Kittur, S. Nayak, B. Murgunde, Binderless nano marigold flower like structure of nickel sulfide electrode for sustainable supercapacitor energy storage applications, J. Energy Storage 62 (2023) 106963.
[9] A. Inman, T. Hryhorchuk, L. Bi, R.J. Wang, B. Greenspan, T. Tabb, E.M. Gallo, A. VahidMohammadi, G. Dion, A. Danielescu, Wearable energy storage with MXene textile supercapacitors for real world use, J. Mater. Chem. A 11 (2023) 3514–3523.
[10] Q. Hassan, A.Z. Sameen, O. Olapade, M. Alghoul, H.M. Salman, M. Jaszczur, Hydrogen fuel as an important element of the energy storage needs for future smart cities, Int. J. Hydrog. Energy 48 (2023) 30247–30262.
[11] R. Kötz, M. Carlen, Principles and applications of electrochemical capacitors, Electrochim. Acta 45 (2000) 2483–2498.
[12] M.G. Kotp, S.U. Sharma, J.-T. Lee, A.F.M. EL-Mahdy, S.-W. Kuo, Triphenylamine-based conjugated microporous polymers as dye adsorbents and supercapacitors, J. Taiwan Inst. Chem. Eng. 134 (2022) 104310.
[13] M. Ahmed, M.G. Kotp, T.H. Mansoure, R.-H. Lee, S.-W. Kuo, A.F.M. EL-Mahdy, Ultrastable carbazole-tethered conjugated microporous polymers for high-performance energy storage, Microporous Mesoporous Mater. 333 (2022) 111766.
[14] B. Yin, L. Hao, X. Li, Q. Yang, CoCx-induced interfacial octahedral Co2+ sites of NiCo-LDH electrode with improved faradic reactivity toward high-performance supercapacitor, J. Colloid Interface Sci. 651 (2023) 602–611.
[15] A. Molaei, X. Crispin, Faradic side reactions at novel carbon flow-through electrodes for desalination studied in a static supercapacitor, Archit., Adv. Sustain. Syst. 4 (2023) 2200119.
[16] M. Minakshi, K. Wickramaarachchi, Electrochemical aspects of supercapacitors in perspective: from electrochemical configurations to electrode materials processing, Prog. Solid State Chem. (2023) 100390.
[17] A. Chatterjee, J. Sun, K.S. Rawat, V. Van Speybroeck, P. Van Der Voort, Exploring the charge storage dynamics in donor–acceptor covalent organic frameworks based supercapacitors by employing ionic liquid electrolyte, Small (2023) 2303189.
[18] S.G. Sayyed, A.V. Shaikh, U.P. Shinde, P. Hiremath, N. Naik, Copper oxide-based high-performance symmetric flexible supercapacitor: potentiodynamic deposition, J. Mater. Sci.: Mater. Electron 34 (2023) 1361.
[19] X. Zheng, H. Yu, R. Xing, X. Ge, H. Sun, R. Li, Q. Zhang, Multi-growth site graphene/polyaniline composites with highly enhanced specific capacitance and rate capability for supercapacitor application, Electrochim. Acta 260 (2018) 504–513.
[20] W. Dong, M. Xie, S. Zhao, Q. Qin, F. Huang, Materials design and preparation for high energy density and high power density electrochemical supercapacitors, Mater. Sci. Eng. R. Rep. 152 (2023) 100713.
[21] L.L. Zhang, X. Zhao, Carbon-based materials as supercapacitor electrodes, Chem. Soc. Rev. 38 (2009) 2520–2531.
[22] M. Maher, S. Hassan, K. Shoueir, B. Yousif, M.E.A. Abo-Elsoud, Activated carbon electrode with promising specific capacitance based on potassium bromide redox additive electrolyte for supercapacitor application, J. Mater. Res. Technol. 11 (2021) 1232–1244.
[23] W. Tian, Q. Gao, Y. Tan, K. Yang, L. Zhu, C. Yang, H. Zhang, Bio-inspired beehive-like hierarchical nanoporous carbon derived from bamboo-based industrial by-

product as a high performance supercapacitor electrode material, J. Mater. Chem. A 3 (2015) 5656–5664.
[24] G. Jiang, R.A. Senthil, Y. Sun, T.R. Kumar, J. Pan, Recent progress on porous carbon and its derivatives from plants as advanced electrode materials for supercapacitors, J. Power Sources 520 (2022) 230886.
[25] K. Jurewicz, K. Babeł, A. Źiółkowski, H. Wachowska, Ammoxidation of active carbons for improvement of supercapacitor characteristics, Electrochim. Acta 48 (2003) 1491–1498.
[26] L. Yang, X. Guo, Z. Jin, W. Guo, G. Duan, X. Liu, Y. Li, Emergence of melanin-inspired supercapacitors, Nano Today 37 (2021) 101075.
[27] X. Xiao, H. Song, S. Lin, Y. Zhou, X. Zhan, Z. Hu, Q. Zhang, J. Sun, B. Yang, T. Li, Scalable salt-templated synthesis of two-dimensional transition metal oxides, Nat. Commun. 7 (2016) 11296.
[28] B. Li, Y. Wang, N. Jiang, L. An, J. Song, Y. Zuo, F. Ning, H. Shang, D. Xia, Electrolytic-anion-redox adsorption pseudocapacitance in nanosized lithium-free transition metal oxides as cathode materials for Li-ion batteries, Nano Energy 72 (2020) 104727.
[29] L. Yan, L. Niu, C. Shen, Z. Zhang, J. Lin, F. Shen, Y. Gong, C. Li, X. Liu, S. Xu, Modulating the electronic structure and pseudocapacitance of δ-MnO2 through transitional metal M (M= Fe, Co and Ni) doping, Electrochim. Acta 306 (2019) 529–540.
[30] A.M. Bryan, L.M. Santino, Y. Lu, S. Acharya, J.M. D'Arcy, Conducting polymers for pseudocapacitive energy storage, Chem. Mater. 28 (2016) 5989–5998.
[31] M.G. Sumdani, M.R. Islam, A.N.A. Yahaya, S.I. Safie, Recent advancements in synthesis, properties, and applications of conductive polymers for electrochemical energy storage devices: a review, Polym. Eng. Sci. 62 (2022) 269–303.
[32] S. Sardana, A. Gupta, K. Singh, A. Maan, A. Ohlan, Conducting polymer hydrogel based electrode materials for supercapacitor applications, J. Energy Storage 45 (2022) 103510.
[33] N. Casado, G. Hernandez, H. Sardon, D. Mecerreyes, Current trends in redox polymers for energy and medicine, Prog. Polym. Sci. 52 (2016) 107–135.
[34] M.M. Ayad, W.A. Amer, M.G. Kotp, I.M. Minisy, A.F. Rehab, D. Kopecký, P. Fitl, Synthesis of silver-anchored polyaniline–chitosan magnetic nanocomposite: a smart system for catalysis, RSC Adv. 7 (2017) 18553–18560.
[35] M.M. Ayad, W.A. Amer, M.G. Kotp, Magnetic polyaniline-chitosan nanocomposite decorated with palladium nanoparticles for enhanced catalytic reduction of 4-nitrophenol, Mol. Catal. 439 (2017) 72–80.
[36] J. Zhang, L. Xu, W.-Y. Wong, Energy materials based on metal Schiff base complexes, Coord. Chem. Rev. 355 (2018) 180–198.
[37] Z. Zhang, Y. Zhou, P. Chen, S. Zeng, W. Nie, Y. Xu, Investigation of capacity increase in schiff-base networks as the organic anode for lithium-ion batteries, ACS Appl. Energy Mater. 4 (2021) 12882–12891.
[38] J.L. Segura, M.J. Mancheño, F. Zamora, Covalent organic frameworks based on Schiff-base chemistry: synthesis, properties and potential applications, Chem. Soc. Rev. 45 (2016) 5635–5671.
[39] L. Xu, F. Wang, X. Ge, R. Liu, M. Xu, J. Yang, Covalent organic frameworks on reduced graphene oxide with enhanced electrochemical performance, Microporous Mesoporous Mater. 287 (2019) 65–70.
[40] X. Zhuang, F. Zhang, D. Wu, X. Feng, Graphene coupled Schiff-base porous polymers: towards nitrogen-enriched porous carbon nanosheets with ultrahigh electrochemical capacity, Adv. Mater. 26 (2014) 3081–3086.
[41] A.B. Asha, Y. Chen, R. Narain, Bioinspired dopamine and zwitterionic polymers for non-fouling surface engineering, Chem. Soc. Rev. 50 (2021) 11668–11683.
[42] M.G. Mohamed, A.F.M. EL-Mahdy, M.G. Kotp, S.-W. Kuo, Advances in porous organic polymers: syntheses, structures, and diverse applications, Mater, Adv 3 (2022) 707–733.
[43] M.G. Kotp, C.-L. Chang, A.F. EL-Mahdy, Tetraphenyl-p-phenylenediamine-based tunable conjugated microporous polymers: Adsorption and photodegradation of hazardous dyestuff in aqueous environments, J. Water Process Eng. 53 (2023) 103675.
[44] M.G. Kotp, N.L. Torad, J. Lüder, A. El-Amir, W. Chaikittisilp, Y. Yamauchi, A.F. M. EL-Mahdy, A phenazine conjugated microporous polymer-based quartz crystal microbalance for sensitive detection of formaldehyde vapors at room temperature: an experiment and density functional theory study, J. Mater. Chem. A 11 (2023) 764–774.
[45] M.G. Kotp, A.F.M. EL-Mahdy, T.-L. Yang, S.-W. Kuo, A pyridinyl-phenanzine conjugated microporous polymer decorated with ultrafine Ag nanoparticles mediates the rapid reduction of nitrophenol, Microporous Mesoporous Mater. 331 (2022) 111669.
[46] M.G. Kotp, A.M. Elewa, A.F.M. EL-Mahdy, H.-H. Chou, S.-W. Kuo, Tunable pyridyl-based conjugated microporous polymers for visible light-driven hydrogen evolution, ACS Appl. Energy Mater. 4 (2021) 13140–13151.
[47] M.G. Kotp, N.L. Torad, H. Nara, W. Chaikittisilp, J. You, Y. Yamauchi, A.F.M. EL-Mahdy, S.-W. Kuo, Tunable thiophene-based conjugated microporous polymers for the disposal of toxic hexavalent chromium, J. Mater. Chem. A 11 (2023) 15022–15032.
[48] J.H. Wang, C.-L. Chang, Z.W. Zhang, A.F.M. EL-Mahdy, Facile metal-free synthesis of pyrrolo [3, 2-b] pyrrolyl-based conjugated microporous polymers for high-performance photocatalytic degradation of organic pollutants, Polym. Chem. 13 (2022) 5300–5308.
[49] L.R. Ahmed, L. Gilmanova, C.-T. Pan, S. Kaskel, A.F. EL-Mahdy, Hollow spherical covalent organic frameworks from nonplanar or planar monomers for the fluorescence detection of telomere dna: role of the 2-(2-Azidoethoxy) ethoxy group, ACS Appl. Polym. Mater. 4 (2022) 9132–9143.
[50] A.F. Saber, K.-Y. Chen, A.F.M. EL-Mahdy, S.-W. Kuo, Designed azo-linked conjugated microporous polymers for CO_2 uptake and removal applications, J. Polym. Res 28 (2021) 430.
[51] Y. Zhi, Z. Wang, H.L. Zhang, Q. Zhang, Recent progress in metal-free covalent organic frameworks as heterogeneous catalysts, Small 16 (2020) 2001070.
[52] L.R. Ahmed, A.F.M. EL-Mahdy, C.-T. Pan, S.-W. Kuo, A water-soluble copper-immobilized covalent organic framework functioning as an "OFF–ON" fluorescent sensor for amino acids, Mater. Adv. (2021) 4617–4629.
[53] A.F.M. EL-Mahdy, J. Lüder, M.G. Kotp, S.-W. Kuo, A. Tröger's, Base-derived covalent organic polymer containing carbazole units as a high-performance supercapacitor, Polymers 13 (2021) 1385.
[54] K. Amin, N. Ashraf, L. Mao, C.F. Faul, Z. Wei, Conjugated microporous polymers for energy storage: recent progress and challenges, Nano Energy (2021) 105958.
[55] W. Yang, B. Huang, L. Li, K. Zhang, Y. Li, J. Huang, X. Tang, T. Hu, K. Yuan, Y. Chen, Covalently sandwiching MXene by conjugated microporous polymers with excellent stability for supercapacitors, Small Methods 4 (2020) 2000434.
[56] T.-L. Yang, J.-Y. Chen, S.-W. Kuo, C.-T. Lo, A.F.M. EL-Mahdy, Hydroxyl-functionalized covalent organic frameworks as high-performance supercapacitors, Polymers 14 (2022) 3428.
[57] S.-J. Park, H. Zhao, G. Ai, C. Wang, X. Song, N. Yuca, V.S. Battaglia, W. Yang, G. Liu, Side-chain conducting and phase-separated polymeric binders for high-performance silicon anodes in lithium-ion batteries, J. Am. Chem. Soc. 137 (2015) 2565–2571.
[58] H. Deng, L. Lin, M. Ji, S. Zhang, M. Yang, Q. Fu, Progress on the morphological control of conductive network in conductive polymer composites and the use as electroactive multifunctional materials, Prog. Polym. Sci. 39 (2014) 627–655.
[59] K. Kalinathan, D.P. DesRoches, X. Liu, P.G. Pickup, Anthraquinone modified carbon fabric supercapacitors with improved energy and power densities, J. Power Sources 181 (2008) 182–185.
[60] L. Xu, R. Shi, H. Li, C. Han, M. Wu, C.-P. Wong, F. Kang, B. Li, Pseudocapacitive anthraquinone modified with reduced graphene oxide for flexible symmetric all-solid-state supercapacitors, Carbon 127 (2018) 459–468.
[61] Y. Xie, T. Fujimoto, S. Dalgleish, Y. Shuku, M.M. Matsushita, K. Awaga, Synthesis, optical properties and charge transport characteristics of a series of novel thiophene-fused phenazine derivatives, J. Mater. Chem. C. 1 (2013) 3467–3481.
[62] C. Gozalvez, J.L. Zafra, A. Saeki, M. Melle-Franco, J. Casado, A. Mateo-Alonso, Charge transport modulation in pseudorotaxane 1D stacks of acene and azaacene derivatives, Chem. Sci. 10 (2019) 2743–2749.
[63] C. de la Cruz, A. Molina, N. Patil, E. Ventosa, R. Marcilla, A. Mavrandonakis, New insights into phenazine-based organic redox flow batteries by using high-throughput DFT modelling, Sustain. Energy Fuels 4 (2020) 5513–5521.
[64] A. Hollas, X. Wei, V. Murugesan, Z. Nie, B. Li, D. Reed, J. Liu, V. Sprenkle, W. Wang, A biomimetic high-capacity phenazine-based anolyte for aqueous organic redox flow batteries, Nat. Energy 3 (2018) 508–514.
[65] C. Wang, X. Li, B. Yu, Y. Wang, Z. Yang, H. Wang, H. Lin, J. Ma, G. Li, Z. Jin, Molecular design of fused-ring phenazine derivatives for long-cycling alkaline redox flow batteries, ACS Energy Lett. 5 (2020) 411–417.
[66] L. Lyu, M. Mahalingam, S. Mousavion, S. Becker, H. Huang, M. Aeschlimann, B. Stadtmüller, Thermal-driven formation of 2D nanoporous networks on metal surfaces, J. Phys. Chem. C. 123 (2019) 26263–26271.
[67] J. Li, Y. Liu, Y. Qian, L. Li, L. Xie, J. Shang, T. Yu, M. Yi, W. Huang, Describing curved–planar π–π interactions: modeled by corannulene, pyrene and coronene, Phys. Chem. Chem. Phys. 15 (2013) 12694–12701.
[68] A. Hayat, M. Sohail, A. El Jery, K.M. Al-Zaydi, S. Raza, H. Ali, Y. Al-Hadeethi, T. Taha, I.U. Din, M.A. Khan, Recent advances in ground-breaking conjugated microporous polymers-based materials, their synthesis, modification and potential applications, Mater. Today 64 (2023) 180–208.
[69] Z.J. Wang, S. Ghasimi, K. Landfester, K.A. Zhang, Photocatalytic suzuki coupling reaction using conjugated microporous polymer with immobilized palladium nanoparticles under visible light, Chem. Mater. 27 (2015) 1921–1924.
[70] X. Hu, Z. Zhan, J. Zhang, I. Hussain, B. Tan, Immobilized covalent triazine frameworks films as effective photocatalysts for hydrogen evolution reaction, Nat. Commun. 12 (1) (2021) 9.
[71] K. Geng, T. He, R. Liu, S. Dalapati, K.T. Tan, Z. Li, S. Tao, Y. Gong, Q. Jiang, D. Jiang, Covalent organic frameworks: design, synthesis, and functions, Chem. Rev. 120 (2020) 8814–8933.
[72] T.-L. Lee, A.M. Elewa, M.G. Kotp, H.-H. Chou, A.F.M. EL-Mahdy, Carbazole-and thiophene-containing conjugated microporous polymers with different planarity for enhanced photocatalytic hydrogen evolution, Chem. Commun. 57 (2021) 11968–11971.
[73] T.A. Gaber, L.R. Ahmed, A.F. EL-Mahdy, Efficient faradaic supercapacitor energy storage using redox-active pyrene–and benzodithiophene-4, 8-dione–tethered conjugated microporous polymers, J. Mater. Chem. A 11 (2023) 19408–19417.
[74] B.T. McAllister, T.B. Schon, P.M. DiCarmine, D.S. Seferos, A study of fused-ring thieno [3, 4-e] pyrazine polymers as n-type materials for organic supercapacitors, Polym. Chem. 8 (2017) 5194–5202.
[75] S. Cong, J. Chen, L. Wang, L. Lan, Y. Wang, H. Dai, H. Liao, Y. Zhou, Y. Yu, J. Duan, Donor functionalization tuning the n-type performance of donor–acceptor copolymers for aqueous-based electrochemical devices, Adv. Funct. Mater. 32 (2022) 2201821.
[76] J. Zhan, A.F. EL-Mahdy, Redox-Active Benzodithiophene-4, 8-dione-Based conjugated microporous polymers for High-Performance faradaic supercapacitor energy storage, Chem. Eng. J. 473 (2023) 145124.
[77] Z. Rhodes, O. Simoska, A. Dantanarayana, K.J. Stevenson, S.D. Minteer, Using structure-function relationships to understand the mechanism of phenazine-

mediated extracellular electron transfer in Escherichia coli, Iscience 24 (2021) 103033.
[78] H. Li, W. Lyu, Y. Liao, Engineering redox activity in conjugated microporous polytriphenylamine networks using pyridyl building blocks toward efficient supercapacitors, Macromol. Rapid Commun. 40 (2019) 1900455.
[79] A.F.M. EL-Mahdy, C.-H. Kuo, A. Alshehri, C. Young, Y. Yamauchi, J. Kim, S.-W. Kuo, Strategic design of triphenylamine-and triphenyltriazine-based two-dimensional covalent organic frameworks for CO 2 uptake and energy storage, J. Mater. Chem. A 6 (2018) 19532–19541.
[80] S.Y. Park, C.W. Kang, S.M. Lee, H.J. Kim, Y.J. Ko, J. Choi, S.U. Son, Nanoparticulate conjugated microporous polymer with post-modified benzils for enhanced pseudocapacitor performance, Chem. Eur. J. 26 (2020) 12343–12348.
[81] L. Mei, X. Cui, Q. Duan, Y. Li, X. Lv, H.-g Wang, Metal phthalocyanine-linked conjugated microporous polymer hybridized with carbon nanotubes as a high-performance flexible electrode for supercapacitors, Int. J. Hydrog. Energy 45 (2020) 22950–22958.